Research Article | Vol. 26, No. 26 | 24 Dec 2018 | OPTICS EXPRESS 34007
Optics EXPRESS

Ptychographic amplitude and phase reconstruction of bichromatic vortex beams

Y. Esashi,[1] C.-T. Liao,[1,*] B. Wang,[1] N. Brooks,[1] K. M. Dorney,[1] C. Hernández-García,[2] H. Kapteyn,[1] D. Adams,[1,3] and M. Murnane[1]

[1]*JILA and Department of Physics, University of Colorado and NIST, 440 UCB, Boulder, Colorado 80309, USA*
[2]*Grupo de Investigación en Aplicaciones del Láser y Fotónica, Departamento de Física Aplicada, University of Salamanca, Salamanca 37008, Spain*
[3]*Current address: Department of Physics, Colorado School of Mines, Golden, Colorado 80401, USA*
**ChenTing.Liao@colorado.edu*

Abstract: We experimentally demonstrate that ptychographic coherent diffractive imaging can be used to simultaneously characterize the amplitude and phase of bichromatic orbital angular momenta-shaped vortex beams, which consist of a fundamental field, together with its copropagating second-harmonic field. In contrast to most other orbital angular momentum characterization methods, this approach solves for the complex field of a hyperspectral beam. This technique can also be used to characterize other phase-structured illumination beams, and, in the future, will be able to be extended to other complex fields in the extreme ultraviolet or X-ray spectral regions, as well as to matter waves.

1. Introduction

Exciting recent advances have made it possible to achieve full control over the wavefront, polarization, and orbital angular momentum of light fields spanning from the THz, through the visible, and also the extreme ultraviolet spectral regions [1,2]. As a result, it is now possible to generate three-dimensional, structured optical fields [3]. Interest in spin-orbit electromagnetic waves carrying a Pancharatnam–Berry phase singularity (i.e. an optical vortex) started about a decade ago [4,5], especially in laterally confined beams with vortex structures. A vortex beam has a helical-shaped wavefront that rotates around its propagation axis, which imparts orbital angular momentum (OAM) [6,7], even at the single photon level [7]. Vortex and OAM beams have been used for applications such as super-resolution microscopy, optical communication, quantum information processing, and optical traps and tweezers [8–13]. In addition to these applications, novel techniques to produce and manipulate OAM beams are being developed. For example, fork holograms, high precision optical components such as spiral phase plates, planar patterned anisotropic media such as liquid crystal q-plates, and spatial light modulators are routinely used to generate OAM beams [14–16].

Although many methods of producing OAM beams exist, there are far fewer techniques that can detect and quantify the topological charge of an OAM beam, i.e. the amount of OAM in the beam. Detection and characterization of the complex wavefront is a prerequisite for any application involving OAM beams, as highly pure beam modes are usually required. The OAM content can be quantitatively measured through interferometry, triangular apertures, or through the use of cylindrical lenses [17–21]. However, many of these methods often only retrieve the average value of the OAM charge and are inadequate when measurements of both the amplitude and phase profile of the field are required with a high spatial resolution, especially if the field is hyperspectral. Wavefront sensing schemes based on Shack–Hartmann wavefront sensors can characterize both the amplitude and phase of wavefronts, and some variants are also able to handle hyperspectral fields [2,22]. However, since these methods use an array of microlenses

#345600 https://doi.org/10.1364/OE.26.034007
Journal © 2018 Received 13 Sep 2018; revised 10 Oct 2018; accepted 11 Oct 2018; published 14 Dec 2018

Optics EXPRESS

or apertures to sample the wavefront, the spatial resolution of the reconstruction is limited by the manufacturing precision of the array.

Fortunately, computational imaging approaches, such as coherent diffraction imaging (CDI) can characterize complex and/or hyperspectral light fields, including vortex beams, with a high spatial resolution [23–30]. In CDI, light diffracts from a sample (either in reflection or transmission) and the scattered light intensity is detected, usually via a charge-coupled device (CCD) camera. A computational phase retrieval algorithm then iteratively solves for the complex field exiting the sample, by satisfying experimental constraints. Ptychography is a particular variant of CDI that makes use of redundant information from multiple diffraction patterns taken from overlapping regions of the sample [25,31]. Ptychographic CDI solves for the complex transmission or reflectivity of the sample, as well as the complex light field that was used as the probe. This feature of ptychography means that it is both a robust microscopy technique, as well as a wavefront sensing technique that can characterize both the amplitude and phase of an arbitrary wave field. In addition, multiplexed ptychography [27,28] allows simultaneous imaging of multi-wavelength probe beams and the corresponding spectral responses of the sample. OAM beams have been characterized using ptychography [30], but only for single-color, low-topological-charge OAM beams and at low spatial resolution.

Here we demonstrate that multiplexed ptychographic CDI can be used as a high spatial resolution, phase-and-amplitude hyperspectral wavefront sensor by simultaneously characterizing an OAM beam together with its frequency-doubled second-harmonic beam. Multiplexed optical characterization techniques such as CDI offer computational routes to wavelength selectivity and hyperspectral wavefront sensing, without the need to spectrally separate the different components of complex light fields. Moreover, due to the redundancy in a single-wavelength ptychography data set, the amount of data required remains approximately constant as the number of wavelengths increases for reasonable bandwidths, resulting in dramatically shorter data acquisition times compared to other hyperspectral metrologies. This approach can be easily applied not only to OAM beams but also to any other complex or structured light fields. Future applications include characterizing broadband OAM illumination in the millimeter-wave [32], terahertz (THz) [33], as well as coherent beams in the extreme ultraviolet (EUV) [34–36] and X-ray [37,38] regions, where spatially resolved reconstructions of the illumination fields have already been demonstrated to provide an invaluable tool for applications in materials and biological sciences [39–46]. We also expect that this technique can be used to characterize electron and neutron vortex beams [47,48] as well as other matter waves.

2. Experimental and simulation results

2.1 Experimental setup

We simultaneously reconstructed the full electric field of bichromatic, linearly polarized OAM beams consisting of a fundamental field with topological charge $\ell = 2$, and its frequency-doubled field carrying topological charge $\ell = 4$. The experimental setup is shown in Fig. 1. A mode-locked Ti:sapphire oscillator produces stable, ultrafast pulses (~40 fs) at a central wavelength $\lambda = 790$ nm, in a TEM_{00} Gaussian mode. These pulses were then sent through a multifaceted spiral phase plate (SPP) of charge $\ell = 2$ (HoloOr VL-220-795-Y-A, 16 steps per phase ramp), generating a fundamental vortex beam with topological charge $\ell = 2$. This beam was then loosely focused into a beta barium borate (BBO) crystal using a thin lens of focal length 50 cm, which generates a second harmonic beam at $\lambda = 395$ nm with charge $\ell = 4$. Both beams simultaneously illuminated a resolution test target (Thorlabs USAF1951), which was scanned to 64 positions on an 8 x 8 semi-random rectilinear grid. The step size of the grid was 80 μm in both directions, on top of which up to 16 μm randomness was added. Both beams had approximate radii of 250 μm, thus providing for an overlap ratio of more than 3, which is sufficient for the algorithm to converge [49]. The field just after the target was Fourier

Optics EXPRESS

transformed via a 6 cm focal length lens and was collected via a complimentary metal-oxide semiconductor (CMOS) camera (Mightex SCN-B013-U) for each target position. Each diffraction pattern was measured with multiple exposure times and then combined in order to extend the dynamic range of the detector. The data was processed using a multicolor ptychography algorithm [27,28] that solved for the complex fields of the two beams at λ = 790 nm and λ = 395 nm, as well as the corresponding complex transmission of the target for each wavelength in about 500 iterations. In the algorithm, the initial guess of the target amplitude was set as an array of unity with flat phase. The initial guess of the beam amplitudes was set as Gaussian with roughly the correct radii, with azimuthal phase wrap of 4π for the fundamental and 8π for the second harmonic. In addition to the usual constraints used in a ptychography algorithm (i.e., overlapping views of the target must agree, and the amplitude of the reconstructed diffracted waves must agree with the measured data), an additional constraint was imposed: the retrieved target must be identical for the two wavelengths modes, since the target does not have any spectrally dependent transmission, namely, it is a binary transmission element.

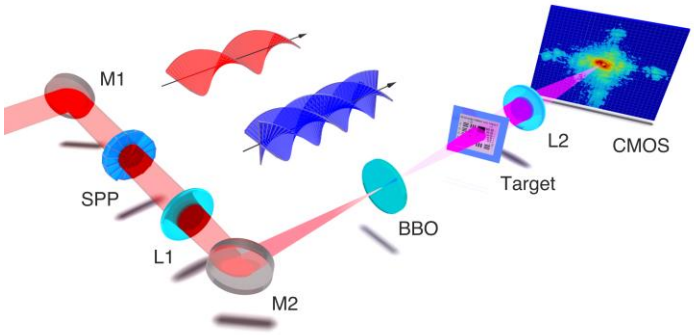

Fig. 1. Experimental schematic for simultaneously imaging an orbital angular momentum beam and its second harmonic. A laser beam with center wavelength 790 nm propagates through a spiral phase plate (SPP) of ℓ = 2 and is focused to a BBO crystal using a lens (L1). The fundamental and second harmonic beams both illuminate a resolution test target, and are Fourier transformed via another lens (L2). The target is moved with respect to the two beams, and diffraction patterns are collected on a CMOS camera. Theoretically rendered helical wavefronts of red (790 nm) and blue (395 nm) OAM beams are shown at the top. M1 and M2: mirrors.

2.2 Simulated and reconstructed wavefronts

The bichromatic OAM beam and the resolution test target were reconstructed from the experimental data using ptychographic CDI, and are shown in Fig. 2. The field amplitude is represented in brightness, while the phase is represented in hue, as indicated by the color wheel in Fig. 2(j). The reconstructed beams in Fig. 2(g) and 2(h) show a clear transfer of topological charge from the fundamental beam (ℓ = 2, phase wrap of 4π) to its second harmonic (ℓ = 4, phase wrap of 8π) [50,51]. A numerical propagation of the experimentally reconstructed beams in Fig. 2(j) and 2(k) show that the fundamental beam propagates through 0 to 2π, while the second harmonic propagates through twice as much phase change, as expected. The propagation was done using the transfer function of free space method. Figures 2(a) and 2(b) show the reconstructed target from experiments at 790 nm and 395 nm, respectively. The two reconstructed targets should be identical, as there is only one resolution target illuminated by both beams, and its transmission has no spectral dependence. Note that the roughness in Fig. 2(b) is due to a reduced signal-to-noise ratio in the second harmonic beam, which is the result of both a lower field amplitude and a reduced quantum efficiency of the CMOS camera at this wavelength.

Optics EXPRESS

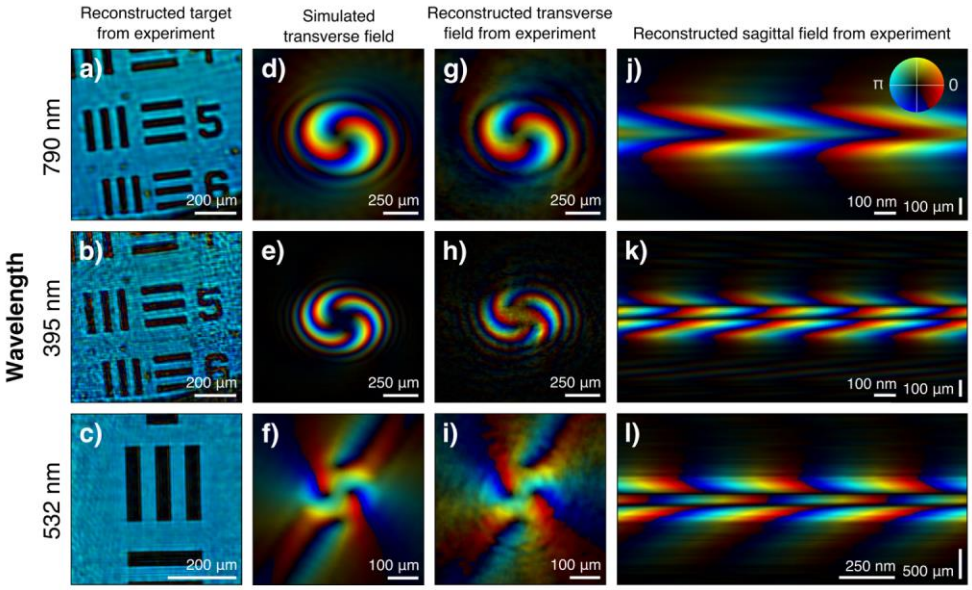

Fig. 2. Reconstructed test target from the experimental data (first column), simulated transverse field at the target (second column), reconstructed transverse field at the target from the experimental data (third column) and sagittal cross section of the reconstructed fields, propagated close to the focus (fourth column) for a bichromatic field (first and second row, λ = 790 nm and λ = 395 nm respectively) and a single-color field (bottom row, λ = 532 nm). In all cases, the electric field amplitude (arbitrary units) is represented in brightness while the phase is represented as a hue, as indicated by the color wheel in (j). In the second column, the transverse fields were simulated by applying the spiral phase plate and the focusing lens phase to an input TEM_{00} Gaussian beam with adjustable radius and phase curvature, and then propagating the field to the location of the target.

There are two and four singularities close to the center of the reconstructed beam profiles in Figs. 2(g) and 2(h), respectively, in contrast to the single singularity expected for a pure Laguerre-Gaussian (LG) mode that theoretically describes OAM beams. These two singularities in the beam profile of the fundamental beam may be due to a slight offset of the laser wavelength to the design wavelength of the SPP at 795 nm, and/or a slight amount of astigmatism of the initial Gaussian beam. Also, it is worth mentioning that a stepped SPP is not able to generate pure LG modes, even from a high quality TEM_{00} Gaussian mode input, and thus the generated vortex beams carry a superposition of OAM charges (i.e., fractional OAM), as analytically described in [52]. This point is further illustrated by performing a modal decomposition of the reconstructed OAM beams into an LG basis. When the reconstructed fundamental beam was numerically decomposed into LG modes of OAM number ℓ between –2 and 6, approximately 80% of the total field was accounted for by LG modes of ℓ = 2. For the second harmonic beam, when decomposed into LG modes of ℓ between –2 and 8, approximately 58% of the total field was accounted for by LG modes of ℓ = 4. To further corroborate this point, we perform an azimuthal Fourier transform over the reconstructed beam profiles, which also recovers the OAM spectrum but without the need for an analytical basis [53]. The OAM spectrum of the two reconstructed fields obtained in this way is shown in Fig. 3(a) for λ = 790 nm and Fig. 3(b) for λ = 395 nm, and high yield is seen at ℓ = 2 for the fundamental beam and at ℓ = 4 for the second harmonic beam, as expected. When the spectrum was integrated along the radius to give the total yield for each ℓ, 33.6% of the field was accounted for by LG mode of ℓ = 2 in the fundamental beam, and 12.4% of the field was accounted for by LG mode of ℓ = 4 in the second harmonic. The lower yields compared to the LG modal decomposition is due to the fact that the OAM spectrum obtained through azimuthal

Optics EXPRESS

Fourier transform was calculated for a wider range of $\ell = \pm 60$, compared to that for the LG modal decomposition.

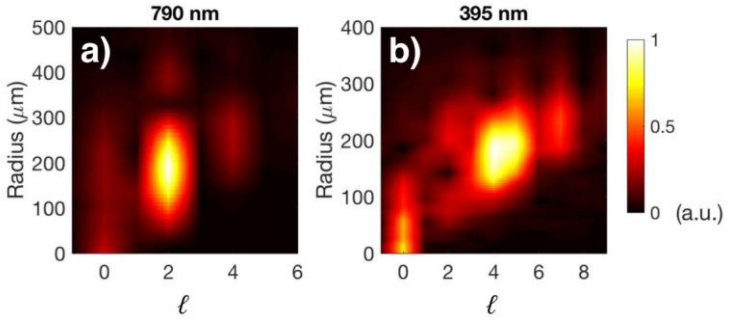

Fig. 3. Retrieved OAM spectrum of the two reconstructed vortex beam fields obtained by Fourier transformation of the fields along the azimuthal direction for different radii, for (a) 790 nm and (b) 395 nm. The color map corresponds to the spectrum in arbitrary units (a.u.). Note that the resolution in the OAM number ℓ is limited to one from Fourier transform of the azimuthal coordinate; the plot has been interpolated for smoothness. In addition, the Fourier transform is in the range $\ell = \pm 60$, but here we present the section of the spectrum with the highest yield. High yield is seen at $\ell = 2$ for $\lambda = 790$ nm and at $\ell = 4$ for $\lambda = 395$ nm as expected.

To test the fidelity of ptychographic CDI as a high spatial resolution wavefront sensor, possible beam profiles at the imaging plane of the experiment were simulated and compared to the experimentally reconstructed beams. The simulation involved (1) applying the SPP and the focusing lens phase to an input TEM_{00} Gaussian beam with adjustable radius and phase curvature, and then (2) propagating the field to the imaging plane (i.e., the location of the target) using the transfer function of free space method. The SPP phase was applied as a discrete 32 stepped phase spiral in two ramps, and the lens phase was approximated as a thin lens without any aberrations. The second harmonic beam was then simulated by squaring the simulated field of the fundamental beam. Within a physically reasonable adjustment range of the parameters involved (the initial input beam radius, phase curvature independently in x and y, and the exact propagation distance between the phase plate-lens system to the target), we obtain simulated fields that agree exceptionally well with the reconstructed fields from the experiment, as they are shown in Fig. 2(d) and 2(e).

To further check the accuracy of our simulation and to improve our understanding, we also present numerical simulation and experimental reconstruction for an additional data set, which we acquired with a single input beam at $\lambda = 532$ nm from a diode-pumped, frequency-doubled Nd:YAG laser (Fig. 2, bottom row). In this case, the laser's wavelength is far from the designed wavelength of the SPP, therefore the output field carries a fractional topological charge and the beam shows a more complicated amplitude and phase profile. Nonetheless, we achieved a high level of agreement between our simulation and experimental reconstruction as shown in Fig. 2(f) and 2(i). We note that the reconstructed target in Fig. 2(c) looks different from Fig. 2(a) and 2(b) because different region of interest were chosen from the target and illuminated by the laser when conducting the singe-color experiment at 532 nm. Generally, the choice of the region of interest from a target does not affect the performance of the ptychographic CDI as long as there are enough spatial structures to constrain the reconstruction algorithm.

2.3 Fidelity tests of the ptychographic reconstructions

As another fidelity test of the ptychographic reconstruction, the experimentally reconstructed, complex field of the fundamental beam was numerically propagated back to a plane just after the SPP position in the experimental setup. At this position, the field amplitude shows a spoke-like pattern that spreads out in the radial direction as shown in Fig. 4(c), where the white lines are shown as a guide to the eye. We separate the reconstructed amplitude and phase of the SPP

Optics EXPRESS

as in Fig. 4(c) and 4(d), respectively, in order to increase the visibility of the spoke-like pattern. This spoke pattern stems from the discrete and stepped nature of our SPP as shown in Fig. 4, where Fig. 4(a) is a 3D sketch of the SPP and Fig. 4(b) is an optical microscope image at the center of the SPP (note that dark lines along certain angles of the SPP are likely slight manufacturing imperfections.) When the field amplitude from Fig. 4(c) was radially integrated as shown in Fig. 4(e), we observe 32 distinct peaks, in agreement with the number of discrete steps in the SPP.

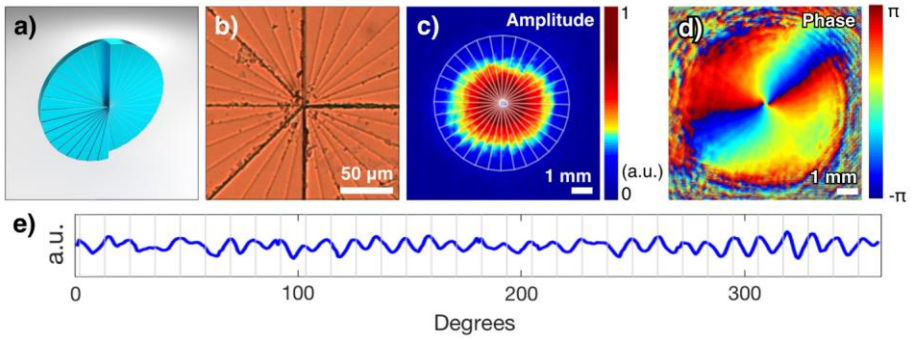

Fig. 4. Extracting the spiral phase plate (SPP) structure from the reconstructed fundamental field. (a) 3D illustration of the SPP geometry, with 32 discrete steps that are applied in two consecutive ramps. (b) Optical microscope image at the center of the SPP. The reconstructed fundamental field from ptychography is numerically propagated to the plane of the SPP, and is shown in (c) amplitude (arbitrary units) and (d) phase. The white lines in (c) are shown as a guide to the eye. The amplitude of the field was radially integrated and is shown in (e). After large period oscillations have been removed for visibility, the number of peaks agrees with the number of discrete steps in the SPP used in the experiment.

The previous analysis demonstrates one of the largest advantages of using ptychography as a high-resolution wavefront sensor: the ability to inspect the full complex beam wavefront at an arbitrary position. This allows for direct visualization of propagation effects as a beam traverses an optical setup, allowing for optimization and diagnosis of optical elements in hard to access positions. In order to demonstrate this unique versatility, we visualize the characteristic, helical wavefronts of the vortex beams from the experimental data by numerically propagating the experimentally reconstructed fields. These beams are visualized in Fig. 5 via surface plots of constant phase, with an intensity threshold. The individual plots in Fig. 5(a) for each wavelength (790 nm: left, red; 395 nm: right, blue) display a clear spiral structure with two planes (of constant phase) for the fundamental beam and four planes for its second harmonic. From these two propagated fields, it is possible to solve for the total electric field of the two beams up to the relative phase between them, which ptychography is not sensitive to. Depending on the relative phase between the two beams, the second harmonic beam can either constructively interfere with the fundamental, resulting in a wavefront that is close to that of the fundamental or, with a slight phase offset, more complicated wavefronts can be obtained, as shown in Fig. 5(b) and 5(c). With additional control over the intensity ratio between the two beams as well as the OAM charge of the fundamental beam, it is possible to synthesize a bichromatic vortex field with unique field configurations. Such beams may be of interest, for example, for manipulating spin and charge dynamics on few-cycle periods, from the picosecond to femtosecond to attosecond timescales, as well as for unique quantum sensing and metrology applications. It is worth noting, however, that bichromatic fields behave as an incoherent sum of two independent fields for timescales greater than their optical periods. These beams may also find applications in areas such as optical tweezers, as the unique beam structures in multicolor OAM beams can yield complex potential energy landscapes as well as locally controllable OAM transfer to trapped objects. Indeed, while interference of same-color OAM beams has been investigated [54,55], properties and applications of superposition of

Optics EXPRESS

different wavelengths OAM beams have remained largely unexplored. As such, ptychographic CDI provides a robust, high resolution method for quantifying complex optical wavefronts for future applications using vortex beams.

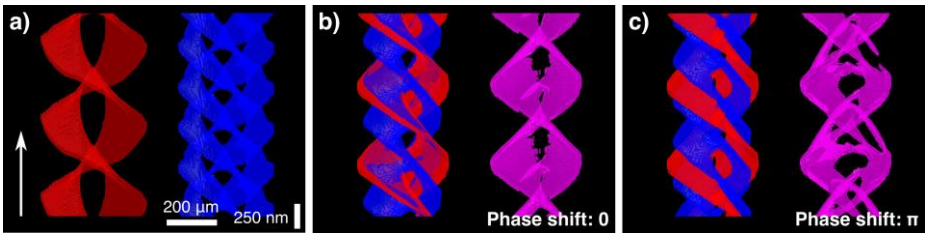

Fig. 5. A constant phase plot of the 3D numerically propagated beams from the experimental reconstructions. (a) shows the fundamental (left, red) and the second harmonic (right, blue) beams individually. In (b) and (c), the fundamental and the harmonic beams are combined with different relative phase shifts (left) to produce contrasting total fields (right, magenta), assuming that two fields have exactly the same amplitude. The arrow in (a) indicates the propagation direction.

3. Conclusion

We have demonstrated that multiplexed, ptychographic CDI can be used as a high-resolution, phase-and-amplitude, hyperspectral wavefront sensor by characterizing both a bichromatic vortex beam carrying OAM and a highly complex, single-color vortex beam consisting of a superposition of several OAM charges. In particular, we have shown that this method is effective in cases where there are OAM beams with different spectral content that are superposed in space and time, which opens the door to applying multi-wavelength ptychography across a broad spectral range. In principle, this characterization method is not strongly wavelength dependent, and can be applied to other spectral ranges where implementing interferometric techniques to characterize OAM content are not trivial such as the THz, EUV, and X-ray regimes, and even electron and neutron beams. In these settings, spatially resolved reconstructions across the entire wavelength (optical, EUV beams) or energy (matter beams) are very useful for applications in spectroscopy, microscopy, and metrology. Finally, we note that this method can be regarded as a general wavefront sensing technique, and so it is very straightforward to characterize other types of structured illumination that are of interest, such as nondiffracting beams, accelerating beams, and other complex light and matter waves for microscopy or optical manipulation purposes.

Funding

The NSF STROBE STC (DMR-1548924); DOE BES AMOS grant (DE-FG02-99ER14982); the NSF GRFP (DGE 1650115); 2017 Leonardo Grant for Researchers and Cultural Creators, BBVA Foundation; Junta de Castilla y León (SA046U16); Ministerio de Economía y Competitividad (FIS2016-75652-P).

References

1. M. Sato, T. Higuchi, N. Kanda, K. Konishi, K. Yoshioka, T. Suzuki, K. Misawa, and M. Kuwata-Gonokami, "Terahertz polarization pulse shaping with arbitrary field control," Nat. Photonics **7**(9), 724–731 (2013).
2. F. Sanson, A. K. Pandey, F. Harms, G. Dovillaire, E. Baynard, J. Demailly, O. Guilbaud, B. Lucas, O. Neveu, M. Pittman, D. Ros, M. Richardson, E. Johnson, W. Li, P. Balcou, and S. Kazamias, "Hartmann wavefront sensor characterization of a high charge vortex beam in the extreme ultraviolet spectral range," Opt. Lett. **43**(12), 2780–2783 (2018).
3. H. Rubinsztein-Dunlop, A. Forbes, M. V. Berry, M. R. Dennis, D. L. Andrews, M. Mansuripur, C. Denz, C. Alpmann, P. Banzer, T. Bauer, E. Karimi, L. Marrucci, M. Padgett, M. Ritsch-Marte, N. M. Litchinitser, N. P. Bigelow, C. Rosales-Guzmán, A. Belmonte, J. P. Torres, T. W. Neely, M. Baker, R. Gordon, A. B. Stilgoe, J. Romero, A. G. White, R. Fickler, A. E. Willner, G. Xie, B. McMorran, and A. M. Weiner, "Roadmap on Structured Light," J. Opt. **19**(1), 013001 (2017).

Optics EXPRESS

4. M. R. Dennis, K. O'Holleran, and M. J. Padgett, "Chapter 5 Singular optics: Optical vortices and polarization singularities," Prog. Opt. **53**, 293–363 (2009).
5. K. Y. Bliokh, F. J. Rodríguez-Fortuño, F. Nori, and A. V. Zayats, "Spin–orbit interactions of light," Nat. Photonics **9**(12), 796–808 (2015).
6. R. A. Beth, "Mechanical detection and measurement of the angular momentum of light," Phys. Rev. **50**(2), 115–125 (1936).
7. L. Allen, M. W. Beijersbergen, R. J. C. Spreeuw, and J. P. Woerdman, "Orbital angular momentum of light and the transformation of Laguerre-Gaussian laser modes," Phys. Rev. A **45**(11), 8185–8189 (1992).
8. F. Tamburini, G. Anzolin, G. Umbriaco, A. Bianchini, and C. Barbieri, "Overcoming the rayleigh criterion limit with optical vortices," Phys. Rev. Lett. **97**(16), 163903 (2006).
9. L. Yan, P. Gregg, E. Karimi, A. Rubano, L. Marrucci, R. Boyd, and S. Ramachandran, "Q-plate enabled spectrally diverse orbital-angular-momentum conversion for stimulated emission depletion microscopy," Optica **2**(10), 900–903 (2015).
10. A. E. Willner, H. Huang, Y. Yan, Y. Ren, N. Ahmed, G. Xie, C. Bao, L. Li, Y. Cao, Z. Zhao, J. Wang, M. P. J. Lavery, M. Tur, S. Ramachandran, A. F. Molisch, N. Ashrafi, and S. Ashrafi, "Optical communications using orbital angular momentum beams," Adv. Opt. Photonics **7**(1), 66–106 (2015).
11. H. He, M. E. J. Friese, N. R. Heckenberg, and H. Rubinsztein-Dunlop, "Direct observation of transfer of angular momentum to absorptive particles from a laser beam with a phase singularity," Phys. Rev. Lett. **75**(5), 826–829 (1995).
12. A. Mair, A. Vaziri, G. Weihs, and A. Zeilinger, "Entanglement of the orbital angular momentum states of photons," Nature **412**(6844), 313–316 (2001).
13. A. M. Yao and M. J. Padgett, "Orbital angular momentum: origins, behavior and applications," Adv. Opt. Photonics **3**(2), 161 (2011).
14. V. Y. Bazhenov, M. V. Vasnetsov, and M. S. Soskin, "Laser beams with screw dislocations in their wavefronts," JETP Lett. **52**, 429–431 (1990).
15. M. W. Beijersbergen, R. P. C. Coerwinkel, M. Kristensen, and J. P. Woerdman, "Helical-wavefront laser beams produced with a spiral phaseplate," Opt. Commun. **112**(5-6), 321–327 (1994).
16. L. Marrucci, C. Manzo, and D. Paparo, "Optical spin-to-orbital angular momentum conversion in inhomogeneous anisotropic media," Phys. Rev. Lett. **96**(16), 163905 (2006).
17. M. S. Soskin, V. N. Gorshkov, M. V. Vasnetsov, J. T. Malos, and N. R. Heckenberg, "Topological charge and angular momentum of light beams carrying optical vortices," Phys. Rev. A **56**(5), 4064–4075 (1997).
18. M. Harris, C. A. Hill, and J. M. Vaughan, "Optical helices and spiral interference fringes," Opt. Commun. **106**(4-6), 161–166 (1994).
19. J. M. Hickmann, E. J. S. Fonseca, W. C. Soares, and S. Chávez-Cerda, "Unveiling a truncated optical lattice associated with a triangular aperture using light's orbital angular momentum," Phys. Rev. Lett. **105**(5), 053904 (2010).
20. S. N. Alperin, R. D. Niederriter, J. T. Gopinath, and M. E. Siemens, "Quantitative measurement of the orbital angular momentum of light with a single, stationary lens," Opt. Lett. **41**(21), 5019–5022 (2016).
21. M. Miranda, M. Kotur, P. Rudawski, C. Guo, A. Harth, A. L'Huillier, and C. L. Arnold, "Spatiotemporal characterization of ultrashort optical vortex pulses," J. Mod. Opt. **64**(sup4), S1–S6 (2017).
22. L. Freisem, G. S. M. Jansen, D. Rudolf, K. S. E. Eikema, and S. Witte, "Spectrally resolved single-shot wavefront sensing of broadband high-harmonic sources," Opt. Express **26**(6), 6860–6871 (2018).
23. D. Sayre, "Some implications of a theorem due to Shannon," Acta Crystallogr. **5**(6), 843 (1952).
24. J. Miao, P. Charalambous, J. Kirz, and D. Sayre, "Extending the methodology of X-ray crystallography to allow imaging of micrometre-sized non-crystalline specimens," Nature **400**(6742), 342–344 (1999).
25. J. M. Rodenburg and H. M. L. Faulkner, "A phase retrieval algorithm for shifting illumination," Appl. Phys. Lett. **85**(20), 4795–4797 (2004).
26. A. M. Maiden and J. M. Rodenburg, "An improved ptychographical phase retrieval algorithm for diffractive imaging," Ultramicroscopy **109**(10), 1256–1262 (2009).
27. P. Thibault and A. Menzel, "Reconstructing state mixtures from diffraction measurements," Nature **494**(7435), 68–71 (2013).
28. D. J. Batey, D. Claus, and J. M. Rodenburg, "Information multiplexing in ptychography," Ultramicroscopy **138**, 13–21 (2014).
29. X. Dong, X. Pan, C. Liu, and J. Zhu, "Single shot multi-wavelength phase retrieval with coherent modulation imaging," Opt. Lett. **43**(8), 1762–1765 (2018).
30. T. Saito, Y. Takeo, and H. Mimura, "Precise characterization of focused vortex beams," Jpn. J. Appl. Phys. **56**(9), 092501 (2017).
31. P. Li and A. M. Maiden, "Ten implementations of ptychography," J. Microsc. **269**(3), 187–194 (2018).
32. G. A. Turnbull, D. A. Robertson, G. M. Smith, L. Allen, and M. J. Padgett, "The generation of free-space Laguerre-Gaussian modes at millimetre-wave frequencies by use of a spiral phaseplate," Opt. Commun. **127**(4-6), 183–188 (1996).
33. J. He, X. Wang, D. Hu, J. Ye, S. Feng, Q. Kan, and Y. Zhang, "Generation and evolution of the terahertz vortex beam," Opt. Express **21**(17), 20230–20239 (2013).
34. C. Hernández-García, A. Picón, J. San Román, and L. Plaja, "Attosecond extreme ultraviolet vortices from high-order harmonic generation," Phys. Rev. Lett. **111**(8), 083602 (2013).

Optics EXPRESS

35. G. Gariepy, J. Leach, K. T. Kim, T. J. Hammond, E. Frumker, R. W. Boyd, and P. B. Corkum, "Creating high-harmonic beams with controlled orbital angular momentum," Phys. Rev. Lett. **113**(15), 153901 (2014).
36. A. Rundquist, C. G. Durfee 3rd, Z. Chang, C. Herne, S. Backus, M. M. Murnane, and H. C. Kapteyn, "Phase-matched generation of coherent soft x-rays," Science **280**(5368), 1412–1415 (1998).
37. A. G. Peele, P. J. McMahon, D. Paterson, C. Q. Tran, A. P. Mancuso, K. A. Nugent, J. P. Hayes, E. Harvey, B. Lai, and I. McNulty, "Observation of an x-ray vortex," Opt. Lett. **27**(20), 1752–1754 (2002).
38. J. Bahrdt, K. Holldack, P. Kuske, R. Müller, M. Scheer, and P. Schmid, "First observation of photons carrying orbital angular momentum in undulator radiation," Phys. Rev. Lett. **111**(3), 034801 (2013).
39. D. F. Gardner, M. Tanksalvala, E. R. Shanblatt, X. Zhang, B. R. Galloway, C. L. Porter, R. Karl, Jr., C. Bevis, D. E. Adams, H. C. Kapteyn, M. M. Murnane, and G. F. Mancini, "Subwavelength coherent imaging of periodic samples using a 13.5 nm tabletop high-harmonic light source," Nat. Photonics **11**(4), 259–263 (2017).
40. E. R. Shanblatt, C. L. Porter, D. F. Gardner, G. F. Mancini, R. M. Karl, Jr., M. D. Tanksalvala, C. S. Bevis, V. H. Vartanian, H. C. Kapteyn, D. E. Adams, and M. M. Murnane, "Quantitative chemically specific coherent diffractive imaging of reactions at buried interfaces with few nanometer precision," Nano Lett. **16**(9), 5444–5450 (2016).
41. C. L. Porter, M. Tanksalvala, M. Gerrity, G. Miley, X. Zhang, C. Bevis, E. Shanblatt, R. Karl, M. M. Murnane, D. E. Adams, and H. C. Kapteyn, "General-purpose, wide field-of-view reflection imaging with a tabletop 13 nm light source," Optica **4**(12), 1552 (2017).
42. B. Zhang, D. F. Gardner, M. D. Seaberg, E. R. Shanblatt, H. C. Kapteyn, M. M. Murnane, and D. E. Adams, "High contrast 3D imaging of surfaces near the wavelength limit using tabletop EUV ptychography," Ultramicroscopy **158**, 98–104 (2015).
43. B. Zhang, D. F. Gardner, M. H. Seaberg, E. R. Shanblatt, C. L. Porter, R. Karl, C. A. Mancuso, H. C. Kapteyn, M. M. Murnane, and D. E. Adams, "Ptychographic hyperspectral spectromicroscopy with an extreme ultraviolet high harmonic comb," Opt. Express **24**(16), 18745–18754 (2016).
44. O. Kfir, P. Grychtol, E. Turgut, R. Knut, D. Zusin, D. Popmintchev, T. Popmintchev, H. Nembach, J. M. Shaw, A. Fleischer, H. Kapteyn, M. Murnane, and O. Cohen, "Generation of bright phase-matched circularly-polarized extreme ultraviolet high harmonics," Nat. Photonics **9**(2), 99–105 (2015).
45. T. Fan, P. Grychtol, R. Knut, C. Hernández-García, D. D. Hickstein, D. Zusin, C. Gentry, F. J. Dollar, C. A. Mancuso, C. W. Hogle, O. Kfir, D. Legut, K. Carva, J. L. Ellis, K. M. Dorney, C. Chen, O. G. Shpyrko, E. E. Fullerton, O. Cohen, P. M. Oppeneer, D. B. Milošević, A. Becker, A. A. Jaroń-Becker, T. Popmintchev, M. M. Murnane, and H. C. Kapteyn, "Bright circularly polarized soft X-ray high harmonics for X-ray magnetic circular dichroism," Proc. Natl. Acad. Sci. U.S.A. **112**(46), 14206–14211 (2015).
46. D. D. Hickstein, F. J. Dollar, P. Grychtol, J. L. Ellis, R. Knut, C. Hernandez-Garcia, D. Zusin, C. Gentry, J. M. Shaw, T. Fan, K. M. Dorney, A. Becker, A. Jaron-Becker, H. C. Kapteyn, M. M. Murnane, and C. G. Durfee, "Non-collinear generation of angularly isolated circularly polarized high harmonics," Nat. Photonics **9**(11), 743–750 (2015).
47. B. J. McMorran, A. Agrawal, I. M. Anderson, A. A. Herzing, H. J. Lezec, J. J. McClelland, and J. Unguris, "Electron vortex beams with high quanta of orbital angular momentum," Science **331**(6014), 192–195 (2011).
48. C. W. Clark, R. Barankov, M. G. Huber, M. Arif, D. G. Cory, and D. A. Pushin, "Controlling neutron orbital angular momentum," Nature **525**(7570), 504–506 (2015).
49. O. Bunk, M. Dierolf, S. Kynde, I. Johnson, O. Marti, and F. Pfeiffer, "Influence of the overlap parameter on the convergence of the ptychographical iterative engine," Ultramicroscopy **108**(5), 481–487 (2008).
50. K. Dholakia, N. B. Simpson, M. J. Padgett, and L. Allen, "Second-harmonic generation and the orbital angular momentum of light," Phys. Rev. A **54**(5), R3742–R3745 (1996).
51. J. Courtial, K. Dholakia, L. Allen, and M. J. Padgett, "Second-harmonic generation and the conservation of orbital angular momentum with high-order Laguerre-Gaussian modes," Phys. Rev. A **56**(5), 4193–4196 (1997).
52. L. Janicijevic and S. Topuzoski, "Gaussian laser beam transformation into an optical vortex beam by helical lens," J. Mod. Opt. **63**(2), 164–176 (2016).
53. L. Rego, J. S. Román, A. Picón, L. Plaja, and C. Hernández-García, "Nonperturbative twist in the generation of extreme-ultraviolet vortex beams," Phys. Rev. Lett. **117**(16), 163202 (2016).
54. A. Aadhi, P. Vaity, P. Chithrabhanu, S. G. Reddy, S. Prabakar, and R. P. Singh, "Non-coaxial superposition of vector vortex beams," Appl. Opt. **55**(5), 1107–1111 (2016).
55. A. A. Kovalev and V. V. Kotlyar, "Orbital angular momentum of superposition of identical shifted vortex beams," J. Opt. Soc. Am. A **32**(10), 1805–1810 (2015).